Response of Tropical Precipitation to Global Warming

DAVID M. ROMPS

Department of Earth and Planetary Sciences, Harvard University, Cambridge, Massachusetts

ABSTRACT

Using high-resolution cloud-resolving simulations with different CO_2 concentrations, local precipitation fluxes are found to obey Clausius–Clapeyron (CC) scaling. Previous studies of the effect of CO_2 concentration on precipitation extremes have used general circulation models, which are poor platforms for studying tropical convection because convection is parameterized. In idealized cloud-resolving simulations, it is possible to identify not only the changes in local precipitation fluxes, but also the factors responsible for those changes.

There are many properties of convection that can change as the atmosphere warms, each of which could produce deviations from CC scaling. These properties include the effective water-vapor gradient, cloud pressure depth, and cloud velocity. A simple theory is developed that predicts the changes in these properties consistent with CC scaling. Convection in the cloud-resolving simulations is found to change as predicted by this theory, leading to an ~20% increase in local precipitation fluxes when the CO_2 concentration is doubled. Overall, an increase in CO_2 leads to more vigorous convection, composed of clouds that are wider, taller, and faster.

1. Introduction

With increasing concentrations of greenhouse gases, many aspects of the climate will change, including precipitation fluxes. It is important, however, to distinguish between two different precipitation fluxes: global and local. We can define the global precipitation flux (kg m^{-2} s^{-1}) as the mean precipitation rate (kg s^{-1}) divided by the entire area (m^2). On the other hand, the local precipitation flux can be loosely defined as the mean precipitation rate divided by the mean area over which it is actively raining. If a fraction σ of the domain is precipitating on average, then the local precipitation flux is equal to the global precipitation flux divided by σ.

As concentrations of greenhouse gases rise, the global precipitation rate over the entire earth is expected to increase because of an increase in net downwelling radiation at the surface (Ramanathan 1981; Boer 1993). This expectation is confirmed by general circulation models (GCM), which find an increase in the range of 3%–15% for a doubling of CO_2 (Boer 1993). Far less

certain is what happens to local precipitation fluxes. The prevailing theory, referred to as Clausius–Clapeyron (CC) scaling, is that the local precipitation flux will increase in proportion to changes in the cloud-base saturation mixing ratio q_v^* (e.g., Allen and Ingram 2002; Trenberth et al. 2003; Held and Soden 2006; Pall et al. 2007). The rationale for this scaling is that the initial amount of water in a convecting parcel is equal to q_v^* at the cloud base. If nothing about convection changes except the initial water content of clouds, then the amount of water condensed by convection should increase in proportion to cloud-base q_v^* as the temperature increases. One of the attractive features of this theory is that it is trivial to calculate the change in q_v^* for a given increase in air temperature. In particular, a 1-K increase in air temperature produces about a 7% increase in q_v^*.

This picture depends implicitly on the assumption that a parcel ascends a distance much larger than the q_v^* scale height. Instead, if a parcel convects undiluted from the cloud base at z_{cb} to some relatively shallow height z_f, then the amount of water vapor condensed by the parcel is proportional to $q_v^*(z_{cb}) - q_v^*(z_f)$, not $q_v^*(z_{cb})$. Since changes in atmospheric temperature will alter the moist adiabatic lapse rate, $q_v^*(z_f)$ will not change in the same proportion as $q_v^*(z_{cb})$, and so neither will $q_v^*(z_{cb}) - q_v^*(z_f)$. In other words, we should expect deviations from

Corresponding author address: David M. Romps, Department of Earth and Planetary Sciences, Harvard University, 416 Geological Museum, 24 Oxford St., Cambridge, MA 02138.
E-mail: davidromps@gmail.com

CC scaling. We know from observations (e.g., Yanai et al. 1973; Ciesielski et al. 2003) and cloud-resolving simulations (e.g., Tompkins and Craig 1999; Romps and Kuang 2010) that convective mass fluxes are not constant with height, so $q_v^*(z_{cb})$ may not be an accurate measure of the water released by convection.

Instead, it has been argued that it is more appropriate to think about the effective gradient $\partial q_v^*/\partial z$ experienced by convecting parcels (O'Gorman and Schneider 2009). For example, if an undiluted, saturated parcel convects from z_{cb} to z_f, then the amount of water condensed by that parcel is equal to the distance $z_f - z_{cb}$ times the average $\partial q_v^*/\partial z$ in that height range. Therefore, if the atmosphere warms, but everything else about the parcel stays the same, including z_{cb} and z_f, then the amount of water condensed will increase in proportion to the effective increase in $\partial q_v^*/\partial z$. Given the change in atmospheric temperature profile, the change in this effective derivative could easily be calculated, providing a theory for the changes in local precipitation fluxes.

Unfortunately, even this modified CC theory could fail in several ways. For example, it may not be true that the distance traveled by the parcel is unchanged as the atmosphere warms. In fact, we expect convective mass fluxes to shift to higher altitudes as the radiative-cooling profile shifts upward with global warming (Hartmann and Larson 2002). It is also possible that, in a warmer world, parcels would condense their water vapor more quickly by ascending at a sufficiently higher speed; evidence for an increase in convective velocities with increased sea surface temperature (SST) has been noted in cloud-resolving simulations (Romps 2008). The precipitation efficiency of clouds may also increase (Lindzen et al. 2001), thereby allowing more of the condensed water to reach the ground. Since we still lack a general theory for the vertical velocity and precipitation efficiency of convection, it is not possible to rule out important changes in these quantities as the atmosphere warms.

Ideally, we would use observations to discern long-term changes in local precipitation fluxes. In the midlatitudes, dense networks of precipitation gauges have been present in some countries for the past century, making such studies possible (e.g., Iwashima and Yamamoto 1993; Karl et al. 1995). In the tropics, however, the geographical predominance of the oceans and the paucity of long-term land-based precipitation data have made it impossible to infer the tropics-wide changes in local precipitation fluxes. Many studies have looked at changes in tropical precipitation using general circulation models (e.g., Gordon et al. 1992; Suppiah 1994; Hennessy et al. 1997; Sun et al. 2007; O'Gorman and Schneider 2009), but the tropical precipitation in those models is generated mainly by the convective parameterizations, in

which we have little faith. Even when simulating the current climate, GCMs disagree dramatically on the probability distribution of local precipitation fluxes in the tropics (Kharin et al. 2007). Therefore, this study investigates changes in local precipitation fluxes in the context of a high-resolution cloud-resolving model, where no convective parameterization is needed. This advantage of cloud-resolving models has led to their recent use in the study of climate sensitivity (Bretherton 2007).

The goal of this paper is to quantify the various influences on the local precipitation flux by studying high-resolution cloud-resolving simulations at three different concentrations of CO_2. Section 2 describes these simulations, which are run with concentrations of carbon dioxide equal to 140, 280, and 560 ppmv. Section 3 introduces two identities that relate the properties of convection to the local and global precipitation fluxes. Using a simple set of assumptions compatible with CC scaling, section 4 presents a scaling theory for the behavior of convection. The diagnostic results and their comparison to the scaling theory are presented in section 5. Section 6 gives a summary and discussion.

2. Simulations

The cloud-resolving simulations are performed using Das Atmosphärische Modell (DAM), which has been described by Romps (2008). DAM is a fully compressible atmospheric model that uses the six-class Lin–Lord–Krueger microphysics (Lin et al. 1983; Lord et al. 1984; Krueger et al. 1995) and the fully interactive Rapid Radiative Transfer Model (RRTM) (Clough et al. 2005; Iacono et al. 2008) for both shortwave and longwave radiation. The magnitude and direction of the top-of-atmosphere (TOA) shortwave radiation flux are set to constant values that provide the average first-of-January equatorial insolation using a zenith angle whose cosine is equal to its insolation-weighted average on that day. This gives a TOA downwelling shortwave flux of 572 W m^{-2} incident at a zenith angle of 43°; note that there is no diurnal cycle. Two trace gases are fed to the radiation scheme: the specified concentration of CO_2 and a tropical ozone sounding that is the same for all simulations. No large-scale forcing, such as advection or divergence, is applied to the atmosphere. The finite-volume advection scheme uses the three-dimensional Uniformly Third-Order Polynomial Interpolation Algorithm (UTOPIA) (Leonard et al. 1993) combined with the three-dimensional, monotonic flux limiter of Thuburn (1996). All of the variables in DAM are treated as double precision, and all prognostic variables are conserved by the finite-volume scheme to within round

off error. The computational domain is three-dimensional and doubly periodic in the horizontal with a free-slip, rigid lid at the upper boundary. The radiation scheme treats the ~20 mb of atmosphere above the lid as an extrapolation of the top layer, thereby including its radiative effect. At the lower boundary, surface fluxes are parameterized with a bulk-flux scheme. Since there is no mean advection in these simulations, a 5 m s^{-1} eastward velocity is added to the local wind speed when calculating the bulk fluxes to simulate the flux enhancement from large-scale flow.

Performing CO_2-doubling experiments in a cloud-resolving model is a computationally expensive endeavor because of the twin requirements of high spatial resolution (to faithfully simulate clouds) and long times (to reach a steady-state climate). To mitigate this expense, the cloud-resolving simulations are run to equilibrium at progressively finer grid spacing, a process that takes several years of model time. This procedure is described in appendix A. The fruits of this labor are three simulations equilibrated over a slab ocean at three different concentrations of CO_2: 140, 280, and 560 ppmv. The model domain is a 25.6-km-wide cube with a grid spacing of 200 m.

All statistics are gathered over the last 40 days of the simulations. Over those 40 days, the mean rate of change of SST in each of the simulations has a magnitude less than 0.2 K yr^{-1}. Over this time period, the mean energy tendency of the ocean–atmosphere system is less than 0.3 W m^{-2} in all three simulations. This is small compared to the ~100 W m^{-2} of latent heating in each of the simulations, and compared to the ~7–15 W m^{-2} differences in latent heating between the three simulations. Since there is no Brewer–Dobson circulation, the stratosphere responds to changes in CO_2 only through radiative adjustment; trends in stratospheric water content are 1% month^{-1}, or less, in all three of the equilibrated simulations.

The three simulations (140, 280, and 560 ppmv) equilibrate at sea surface temperatures of 297.5, 300.1, and 303.0 K. This reflects a climate sensitivity in these simulations of about 2.6–2.9 K per doubling of CO_2. Figure 1 displays the temperature, temperature anomaly (from the 140-ppmv simulation), relative humidity (with respect to water for $T \geq 273.16$ K and with respect to ice for $T < 273.16$ K), and parcel buoyancy profiles for the three simulations; the colors blue, black, and red correspond to 140, 280, and 560 ppmv.

Although these simulations were designed with theoretical simplicity in mind, they match—at least qualitatively—the observed and predicted properties of the tropical western Pacific atmosphere. The gray lines in the upper-left, lower-left, and lower-right panels of Fig. 1 show the temperature, relative humidity, and parcel buoyancy

from the mean of 5597 Atmospheric Radiation Measurement Program (ARM) soundings at Manus (2°S, 147°E). The gray line in the upper-right panel is the annual-mean temperature change over Manus averaged over 10 pairs (modern and doubled CO_2) of equilibrium GCM runs performed for the fourth assessment report of the Intergovernmental Panel on Climate Change (IPCC) and archived by the World Climate Research Programme's (WCRP) Coupled Model Intercomparison Project phase 3 (CMIP3) multimodel dataset (Meehl et al. 2007).

The upper-left panel of Fig. 1 shows that the tropospheric temperatures at Manus lie mostly between the temperatures of the 280- and 560-ppmv simulations. In addition, the height of Manus' cold point lies between the cold points of the two simulations. The largest discrepancy is in the temperature of the tropopause: the soundings over Manus have a temperature minimum of 192 K compared to the minima of 198 and 200 K in the two simulations. As seen from the lower-left panel, the simulations' profiles of relative humidity match the qualitative features of the tropical atmosphere with local maxima near the cloud base, the melting line, and the tropopause. Quantitatively, however, the simulations are significantly more humid than the annual mean at Manus. This is to be expected, as there is no synoptic or mesoscale variability in the simulations that could generate dry spells; indeed, the simulations are constantly convecting. In the lower-right panel, we see that the simulations exhibit more convective available potential energy (CAPE) and less convective inhibition (CIN). Again, this is likely attributable to the lack of synoptic and mesoscale variability, which, in the real world, can shut off convection by reducing CAPE and enhancing CIN. In the upper-right panel, a doubling of CO_2 (from 140 to 280 ppmv) in the cloud-resolving simulation generates a temperature change (black line) that agrees quite well with that predicted by the ensemble of GCM runs.

3. An IPAT equation

In the 1970s, Commoner (1971) and Ehrlich and Holdren (1972) introduced a simple equation to help diagnose the causes of environmental impact. Referred to as the "IPAT" equation, it states that environmental impact I is equal to the population P times the per-capita affluence A times the technology T employed. By defining A as dollars per person and T as impact per dollar, the equation $I = PAT$ becomes an identity. Despite its simplicity, this equation has served as a useful starting point for discussing the root causes of environmental impact.
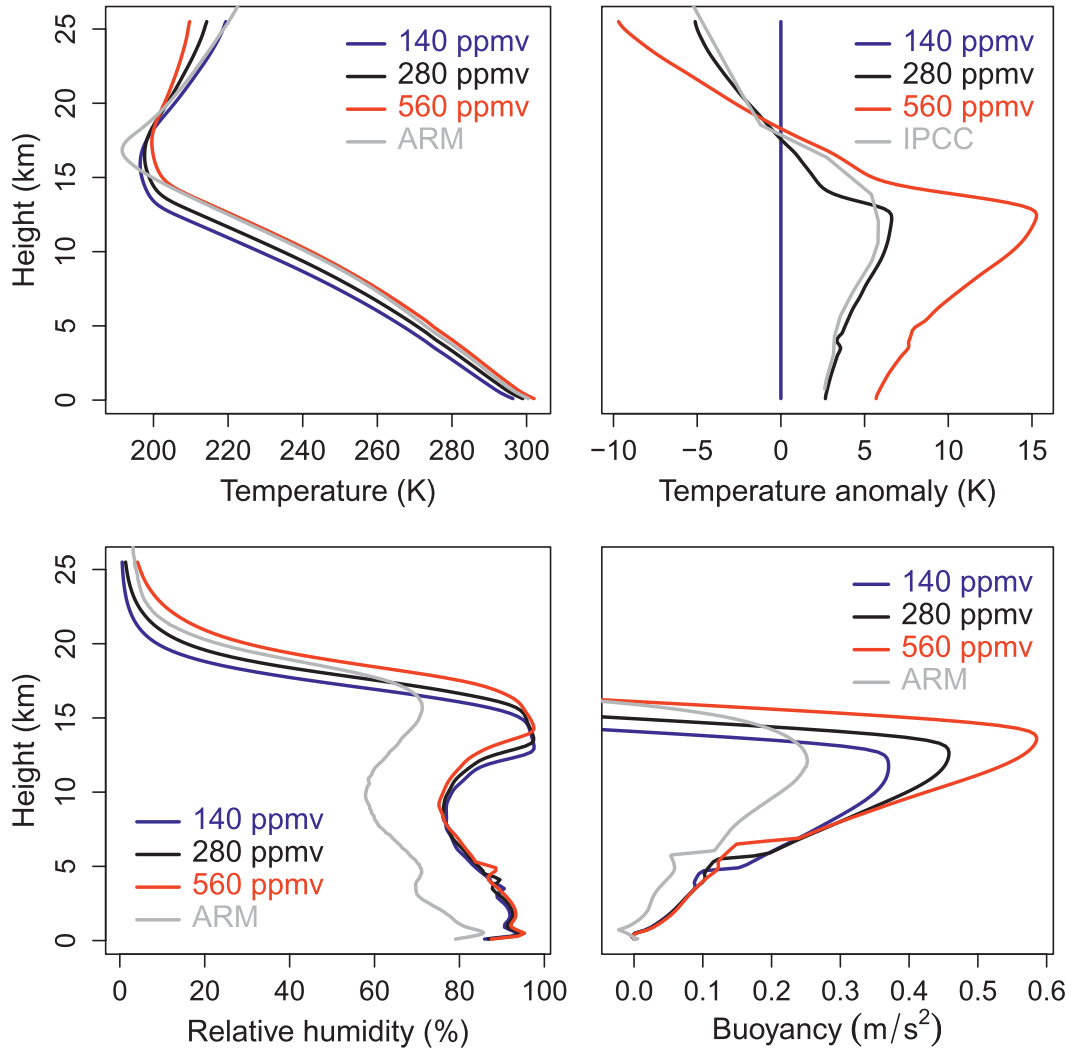
FIG. 1. For 140 (blue), 280 (black), and 560 ppmv (red), the (top left) mean temperature, (top right) mean temperature anomaly from the 140-ppmv case, (bottom left) mean relative humidity, and (bottom right) buoyancy of a parcel lifted—adiabatically and with the latent heat of fusion—through the mean sounding from 100 m. The gray lines are the mean annual profiles over Manus obtained from ARM soundings and, for the temperature anomaly, from 10 pairs (modern and doubled CO_2) of IPCC GCM runs.

In this section, we seek an IPAT-like formula for local and global precipitation fluxes. We will begin by deriving the condensation rate within a small Lagrangian parcel of condensing cloud. Let us define the condensation rate c (kg m^{-3} s^{-1}) to be the nonnegative microphysical sink of water vapor, either through condensation or deposition. By definition, c is zero where there is a net microphysical source of water vapor. To first approximation, c in a condensing parcel can be described by one-dimensional advection:

$$c = -\frac{d}{dt}(q_v \rho) \simeq \rho w \frac{\partial q_v}{\partial z}.$$

This is only approximate because we have neglected diffusion, horizontal advection, and storage. To account for this, we define ϵ_c as the condensation efficiency, given by the ratio of c to $-\rho w \partial q_v / \partial z$, which we expect will be close to one for a condensing parcel. With these definitions, an IPAT equation for the parcel's condensation rate would be

$$c = \epsilon_c \left(-\frac{\partial q_v}{\partial z} \right) \rho w \quad \text{(for a condensing parcel).} \quad (1)$$

For our purposes, parcel-by-parcel statistics provide much more information than we need. Since the

precipitation flux p is a function of $\{x, y, t\}$, we are more interested in the vertically averaged properties of clouds, not the properties of individual parcels. To weight parcels according to their contribution to the hydrologic cycle, we will use condensation-weighted vertical averages; further discussion of this choice may be found in appendix B. In particular, for some function $F = F(x, y, z, t)$, we define the condensation-weighted column average $\overline{F}$ as

$$\overline{F} \equiv \frac{\int dz\, c\, F}{\int dz\, c}.$$

Like the precipitation flux, $\overline{F}$ is a function of $\{x, y, t\}$.

Let us derive an IPAT equation for column-integrated condensation, beginning with the vertically averaged advection term $\overline{-\rho w \partial q_v / \partial z}$. To obtain a condensation efficiency ϵ_c, we must divide the averaged condensation by this advection term: $\epsilon_c \equiv \overline{c}/(\overline{-\rho w \partial q_v / \partial z})$. To get an average water-vapor gradient γ, we must divide the advection term by the averaged mass flux: $\gamma \equiv (\overline{-\rho w \partial q_v / \partial z})/\overline{\rho w}$. The average vertical velocity $\mathbf{w}$ is then given by the mass flux divided by the averaged density: $\mathbf{w} \equiv \overline{\rho w}/\overline{\rho}$. To complete an IPAT equation for column-integrated condensation that is analogous to Eq. (1), we must define a cloud mass m such that

$$\int dz\, c = \epsilon_c \gamma m \mathbf{w} \quad \text{(for a column)}. \qquad (2)$$

Note that m must have units of kilograms per meter squared; it is an effective mass of cloud per surface area of the column. Solving Eq. (2) for m, we find that $m = H\overline{\rho}$, where $H \equiv \int dz\, c / \overline{c}$ is the effective depth of cloud. To give a feel for some of these vertically averaged quantities, Fig. 2 displays some of these fields averaged over a randomly selected 5-min period of the 280-ppmv simulation. The fields are p (upper left), $\int dz\, c$ (upper right), m (lower left), and $\mathbf{w}$ (lower right).

Ultimately, our goal is to define an IPAT equation for the entire radiative–convective equilibrium (RCE). This requires that we average these column-integrated statistics in both the horizontal plane and in time. Over what subset of the horizontal plane should we average? One choice would be the subset of the plane over which $\int dz\, c > 0$, but this could include a large area of lightly condensing clouds. Since our interest is in convection, we will use a subset $A_c(f)$ defined as the area that contains the most intense fraction f of condensation. Closely related is the condensation threshold $C_0(f)$ for columns, which we define such that a fraction f of condensation

occurs in columns with $\int dz\, c > C_0(f)$. Given f, the following two equations define $A_c(f)$ and $C_0(f)$:

$$A_c(f) = \left\{ x, y, t; \int dz\, c(x, y, z, t) > C_0(f) \right\}, \qquad (3)$$

$$\int_{A_c(f)} dt\, dx\, dy \int dz\, c \equiv \int dt\, dx\, dy\, \mathcal{H}\left[\left[\int dz\, c - C_0(f) \right] \int dz\, c \right]$$

$$= f \int dt\, dx\, dy\, dz\, c, \qquad (4)$$

where $\mathcal{H}$ is the Heaviside unit step function. As explained in detail in appendix B, the vertically averaged cloud properties are averaged over $A_c(f)$, which then makes ϵ_c, γ, m, and $\mathbf{w}$ functions only of f; that is, $\epsilon_c = \epsilon_c(f)$, $\gamma = \gamma(f)$, etc. For example, $\mathbf{w}(0.9)$ is the average vertical velocity for most of the simulation's convection. On the other hand, $\mathbf{w}(0.1)$ is the velocity for the most heavily condensing convection, which will tend to be larger than $\mathbf{w}(0.9)$. Similarly, we can define $A_p(f)$ as the area through which falls the most intense fraction f of precipitation,

$$A_p(f) = \left\{ x, y, t; \quad p(x, y, t) > P_0(f) \right\}, \qquad (5)$$

$$\int_{A_p(f)} dt\, dx\, dy\, p \equiv \int dt\, dx\, dy\, \mathcal{H}[p - P_0(f)]p$$

$$= f \int dt\, dx\, dy\, p. \qquad (6)$$

To connect the amount of condensation given by the product $\epsilon_c \gamma m \mathbf{w}$ to the local precipitation flux, we need to define precipitation efficiency. We will define the precipitation efficiency ϵ_p as the average mass of rain that falls through $A_p(f)$ divided by the average mass of water condensed above $A_c(f)$. The implicit assumption here is that the most heavily condensing fraction f of condensation falls to the ground as the most heavily falling fraction f of precipitation. This is equivalent to assuming that ϵ_p is independent of f. This assumption is made necessary by the impracticality of tracking all condensed water to its fate of either fallout or evaporation. As discussed in section 6, the assumption of an f-independent ϵ_p is likely satisfactory for our purposes.

We are now in a position to give rigorous definitions for the local precipitation flux P_l and the global precipitation flux P_g. We define P_l as the mean precipitation flux (kg m^{-2} s^{-1}) through $A_p(f)$. Note that P_l depends implicitly on f, just as ϵ_c, γ, m, and $\mathbf{w}$ do. We define P_g as the mean precipitation flux over the entire domain, which is independent of f. Note that P_g and P_l are normalized differently, as is appropriate for global versus local fluxes:
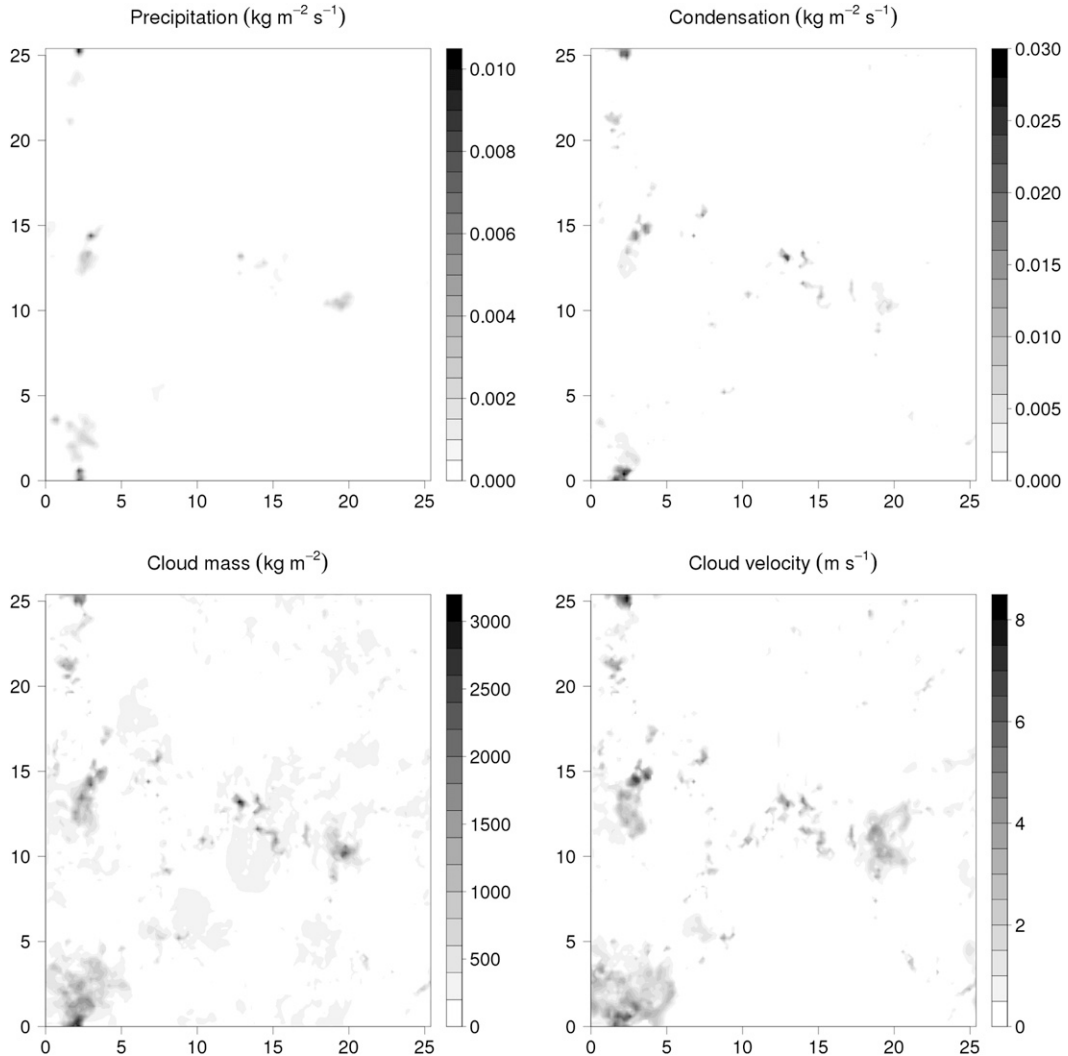
FIG. 2. Snapshots of (top left) p, (top right) $\int dz c$, (bottom left) m, and (bottom right) $\mathbf{w}$. The axes are the x and y axes of the domain (km).

$$P_g \equiv \frac{\int dt\, dx\, dy p}{\int dt\, dx\, dy}, \quad P_l \equiv \frac{\int_{A_p} dt\, dx\, dy p}{\int_{A_p} dt\, dx\, dy}.$$

Also note that fP_g is the contribution to the global precipitation flux from $A_p(f)$. Finally, defining n as the average number of rain events (i.e., connected spaces in a time slice of A_p) per domain area, and defining a as the average area of those rain events, we can write down two IPAT equations for the local and global precipitation fluxes:

$$P_l = \epsilon_p \epsilon_c \gamma m \mathbf{w}, \tag{7}$$

$$fP_g = naP_l. \tag{8}$$

Note that all of the terms in these equations, except ϵ_p and P_g, are functions of f. So long as the fractional changes in the various terms are small, the changes in P_l and P_g can be written as

$$\frac{\delta P_l}{P_l} \approx \frac{\delta \epsilon_p}{\epsilon_p} + \frac{\delta \epsilon_c}{\epsilon_c} + \frac{\delta \gamma}{\gamma} + \frac{\delta m}{m} + \frac{\delta \mathbf{w}}{\mathbf{w}}, \tag{9}$$

$$\frac{\delta P_g}{P_g} \approx \frac{\delta n}{n} + \frac{\delta a}{a} + \frac{\delta P_l}{P_l}. \tag{10}$$

These equations tell us how changes to P_l and P_g (at a fixed f) are related to changes in cloud properties as we alter some physical parameter, such as the concentration of CO_2.

4. A scaling theory

The theory of Clausius–Clapeyron scaling for local precipitation fluxes is predicated on two assumptions:

1) convecting parcels transit from the cloud base to the upper troposphere, and
2) as the atmosphere warms, nothing about convection changes except its water content.

As a result of assumption 1, the amount of water condensed by a convecting parcel is proportional to q_v^* of the surface air. By assumption 2, there are no changes in either the convective mass flux or the precipitation efficiency, so the local precipitation flux is also proportional to q_v^*. This gives the standard Clausius–Clapeyron scaling: $\delta P_l / P_l = \delta q_v^* / q_v^*$.

By strengthening assumption 1, we can build a scaling theory for the other fractional changes in Eq. (9). We strengthen assumption 1 as follows:

1') convection behaves as a steady-state one-dimensional advection from the cloud base to the upper troposphere.

Assumption 1' implies that the convective mass flux ρw is constant with height and the local condensation efficiency $c/(-\rho w \partial q_v / \partial z)$ is unity. By assumption 2, ϵ_p and ρw do not change with warming. The expression for γ can then be written as

$$\gamma \equiv \frac{\overline{-\rho w \dfrac{\partial q_v}{\partial z}}}{\overline{\rho w}} \quad \text{(definition of } \gamma)$$

$$= -\overline{\frac{\partial q_v}{\partial z}} \quad \text{(constant mass flux)}$$

$$= -\frac{\int dz \left(\dfrac{\partial q_v}{\partial z}\right)^2}{\int dz \dfrac{\partial q_v}{\partial z}} \quad \text{(unit condensation efficiency)}$$

$$= -\frac{\int dz \left(\dfrac{\partial q_v^*}{\partial z}\right)^2}{\int dz \dfrac{\partial q_v^*}{\partial z}} \quad \text{(saturated cloud).}$$

Here, the integral over z is taken from the cloud base to the cold-point tropopause. Since q_v^* decreases exponentially with height, the integral is insensitive to the upper bound so long as it is chosen in the upper troposphere.

In a similar way, we can derive theoretical expressions for m and $\mathbf{w}$. The theoretical predictions are as follows:

$$P_l \propto q_v^* \text{ at cloud base,} \tag{11}$$

$$\epsilon_p = \text{constant,} \tag{12}$$

$$\epsilon_c = 1, \tag{13}$$

$$\gamma = -\frac{\int dz \left(\dfrac{\partial q_v^*}{\partial z}\right)^2}{\int dz \dfrac{\partial q_v^*}{\partial z}}, \tag{14}$$

$$m = \frac{\left(\int dz \rho \dfrac{\partial q_v^*}{\partial z}\right)\left(\int dz \dfrac{\partial q_v^*}{\partial z}\right)}{\int dz \left(\dfrac{\partial q_v^*}{\partial z}\right)^2}, \quad \text{and} \tag{15}$$

$$\mathbf{w} \propto \frac{\int dz \dfrac{\partial q_v^*}{\partial z}}{\int dz \rho \dfrac{\partial q_v^*}{\partial z}}. \tag{16}$$

Note that these are the expressions for $\epsilon_p, \epsilon_c, \gamma, m$, and $\mathbf{w}$ that are consistent with a CC scaling of local precipitation fluxes: the product $\epsilon_p \epsilon_c \gamma m \mathbf{w}$ is proportional to $-\int dz \partial q_v^* / \partial z$, which equals q_v^* at the cloud base. Given the mean profiles of q_v^* and ρ, we can calculate these theoretical values for any atmosphere.

5. Results

To make the size of the output manageable, the condensation-weighted integrals for each column are saved as 5-min averages. Since 5 min is short compared to the 1-h time scale of deep convective clouds, little information is lost by averaging in this way. The result, then, is a set of two-dimensional arrays for each 5-min interval of each simulation; these arrays are listed in appendix B. With these data, the values of $P_g, n, a, P_l, \epsilon_p, \epsilon_c, \gamma, m$, and $\mathbf{w}$ are calculated from the last 40 days of each simulation using the thresholds of $f = 0.9$ and $f = 0.1$.

Table 1 gives the values of these quantities for the simulation with a preindustrial CO_2 concentration of 280 ppmv. In this simulation P_g is about 1170 mm yr^{-1}. Using $f = 0.9$, 90% of this precipitation is found to be generated by an average of about $n = 0.035$ precipitation events per kilometer squared, each with an average area a of 0.85 km^2. These precipitation events cover an average fractional area (i.e., mean area of A_p divided by domain area) of $na = 3.1\%$; the corresponding fractional area covered by A_c is 3.6%. The events have an average P_l of 1.1×10^{-3} kg m^{-2} s^{-1}, which is 4 mm h^{-1}. The hydrostatic pressure depth of the convecting clouds, obtained by multiplying m by the gravitational acceleration, is 80 mb. The average vertical velocity w is 3.4 m s^{-1}. Using $f = 0.1$ to focus on the 10% of the precipitation that falls with the highest fluxes, we see

TABLE 1. Numerical values of the terms in Eqs. (7) and (8) for the simulation with 280 ppmv of CO_2. All values are in mks units; in particular, $[P_g] = [P_l] = $ kg m^{-2} s^{-1}, $[n] = $ m^{-2}, $[a] = $ m^2, $[\epsilon_p] = [\epsilon_c] = 1$, $[\gamma] = $ m^{-1}, $[m] = $ kg m^{-2}, and $[\mathbf{w}] = $ m s^{-1}.

f	fP_g	n	a	P_l	ϵ_p	ϵ_c	γ	m	$\mathbf{w}$
90%	3.3×10^{-5}	3.5×10^{-8}	8.5×10^{5}	1.1×10^{-3}	0.21	1.05	1.8×10^{-6}	8.1×10^{2}	3.4
10%	3.7×10^{-6}	2.6×10^{-9}	1.6×10^{5}	8.7×10^{-3}	0.21	0.99	1.9×10^{-6}	3.7×10^{3}	5.9

that n is only 0.0026 km^{-2}. Those events have a of only 0.16 km^2, which is equivalent to a 400-m-wide square; these are likely generated by the cores of deep convective clouds. The fractional areas covered by A_p and A_c are 0.04% and 0.07%, respectively. Under these cores P_l is 31 mm h^{-1}. The cores have an average hydrostatic pressure depth gm of 360 mb and an average speed $\mathbf{w}$ of 5.9 m s^{-1}.

a. Changes in convection

As the CO_2 concentration is doubled, the global precipitation rate increases from 1081 ± 13 mm yr^{-1} at 140 ppmv, to 1166 ± 13 mm yr^{-1} at 280 ppmv, to 1279 ± 22 mm yr^{-1}. The errors given here and in the remainder of this section correspond to the standard error of the mean, which is calculated from time series of daily averages. Figure 3 shows the probability distribution of local precipitation fluxes in each of the three simulations. The solid lines are calculated by smoothing the data with a triangular weighting function whose width increases as it moves up the x axis. The general trend is a shift of the distribution to higher precipitation fluxes as CO_2 increases. This shift to the right generates large fractional increases in probability for the largest precipitation fluxes. For example, the probability of 60 mm h^{-1} precipitation fluxes more than doubles for every doubling of CO_2.

To understand what is driving this trend toward larger local fluxes, we can turn to Eq. (7). Let us begin by considering $f = 0.9$; that is, we include everything but the 10% of precipitation that falls most lightly. The gray bars in the top row of Fig. 4 show the fractional changes in $P_l(0.9)$, $\epsilon_p(0.9)$, etc. as CO_2 is increased from 140 to 280 ppmv (left column) and from 280 to 560 ppmv (right column). We see that P_l increases by 15% and 19% (6% K^{-1}), respectively. We also see that the changes in ϵ_p and ϵ_c are virtually zero, thereby accounting for practically none of the observed changes in P_l. Instead, the increases in P_l are made possible by changes in three quantities in roughly equal measure: γ (+5% and +6%, respectively), m (+4% and +4%), and $\mathbf{w}$ (+5% and +6%). In other words, the local precipitation fluxes increase when CO_2 is increased because clouds travel up a steeper gradient in q_v^*, the clouds are bigger, and the clouds are moving faster. Also, P_g, which is constrained by the surface energy budget, experiences smaller

increases of only 8% and 10% (3% K^{-1}). As we see from Eq. (8), this is compatible with the larger increases in P_l because the total area of precipitation events (i.e., $n \times a$) decreases.

When we focus on the 10% of precipitation that falls most heavily by using $f = 0.1$, we find the fractional changes in $P_l(0.1)$, $\epsilon_p(0.1)$, etc. shown by the gray bars in the bottom row of Fig. 4. Here, we see somewhat larger increases in P_l as CO_2 is doubled. The fractional changes in P_l are +20% and +21% (7%–8% K^{-1}) for the two doublings, compared to +15% and +19% for $f = 0.9$. Again, these increases are made possible by increases in γ (5% and 5%), m (8% and 5%), and $\mathbf{w}$ (5% and 7%). We also see that a increases by about 4% and 13% while n decreases by 14% and 20%. In other words, the most intense precipitation events are generated by convective plumes that are larger, faster, and wider, but they are much less frequent.

The results given so far have been calculated using 5-min averages of local precipitation fluxes and column-integrated quantities. Since unorganized tropical plumes have a lifetime on the order of an hour, an hourly
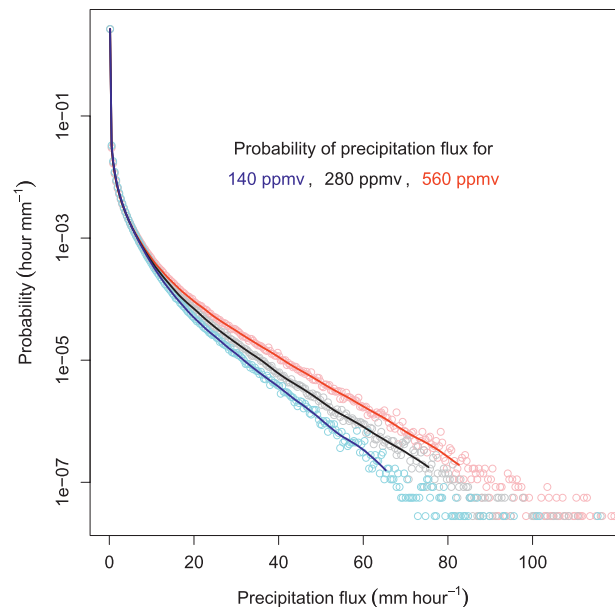
FIG. 3. The probability, or occurrence frequency, of pointwise precipitation rates for the 140- (blue), 280- (black), and 560-ppmv (red) simulations. The lines are running means with a triangular window whose width increases as it moves up the x axis.
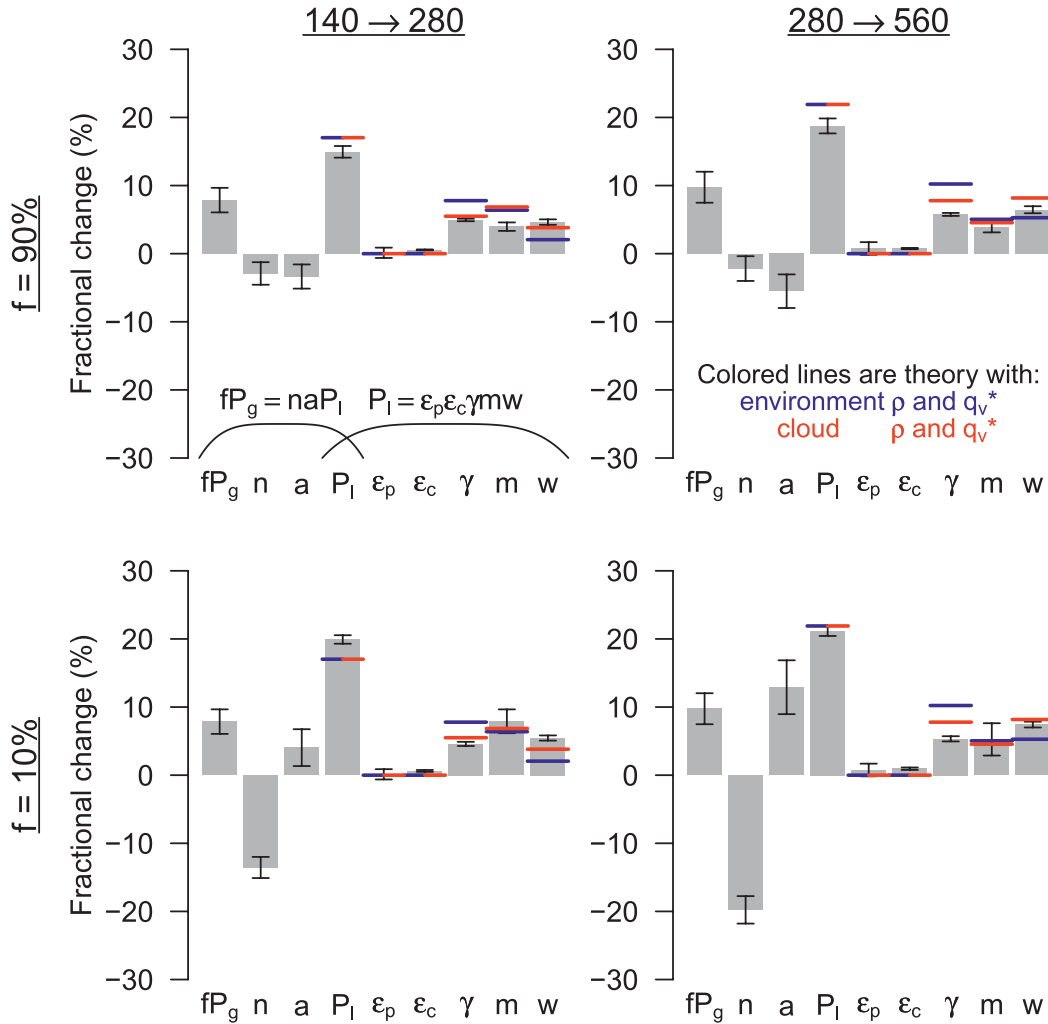
FIG. 4. (top) Fractional changes of each term in Eqs. (7) and (8) calculated using 5-min averages and the $f = 90\%$ threshold. The changes are (left) from 140 to 280 and (right) from 280 to 560 ppmv. (bottom) As at (top), but for the $f = 10\%$ threshold. The colored lines indicate the changes predicted by the theory presented in section 4. The blue lines are calculated using the mean environmental profiles of ρ and q_v^*, while the red lines are calculated using the profiles of ρ and q_v^* for a cloud parcel lifted from the cloud base.

average would give a clearer picture of the total amount of rain dumped by a cloud, not just its instantaneous intensity. Therefore, we aggregate the 5-min data into hourly data by beginning with the 5-min-averaged data arrays, averaging them 12 at a time, and then calculating $P_l(f)$, $\epsilon_p(f)$, etc. as before. The fractional changes for this hourly data are shown in Fig. 5. We see that the results are very similar to the results from the 5-min data. Again, a doubling of CO_2 leads to an $\sim 20\%$ increase in local precipitation fluxes, which are made possible by increases in γ, m, and $\mathbf{w}$. And, for the most intense 10% of precipitation, the number of precipitation events decreases while the area of individual events increases.

b. Comparison to theory

Given the mean profiles of ρ and q_v^* for each of the three simulations, we can use Eqs. (11)–(16) to calculate the fractional changes in convective properties that would naturally give CC scaling of P_l. These changes are indicated by the blue lines in Figs. 4 and 5. We see that these theoretical predictions agree qualitatively with the diagnosed changes in convection. The theory predicts an increase in P_l of about 20% and increases in γ, m, and $\mathbf{w}$ in the range of 2%–10%.

Nevertheless, there are two systematic differences between the theoretical predictions in blue and the observed changes in gray. One is that the theory consistently
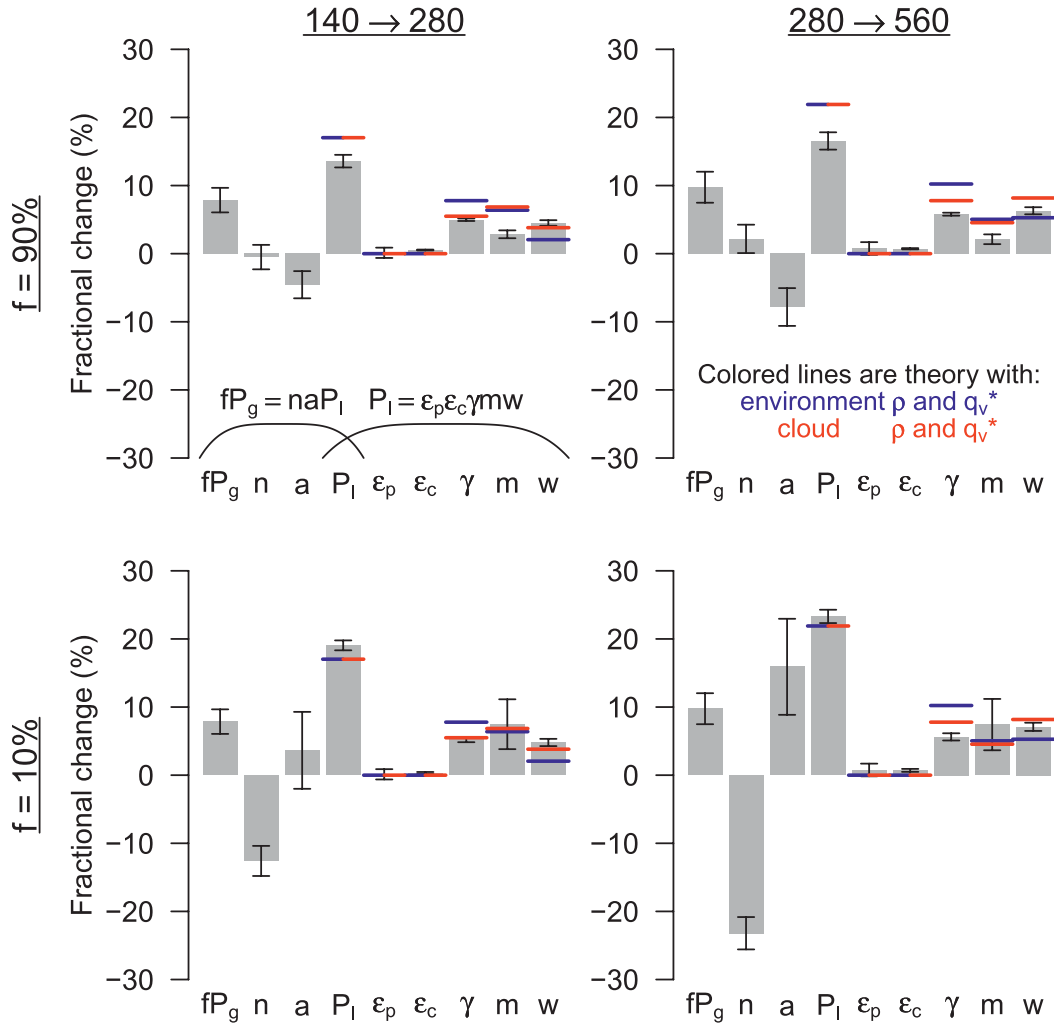
FIG. 5. As in Fig. 4, but for hourly statistics.

overestimates the increase in γ, and the other is that the theory consistently underestimates the increase in **w**. The likely reason for this discrepancy is that convecting clouds are warmer than their surroundings. Clouds begin their life saturated at the cloud base with roughly the same temperature as the surroundings (Romps and Kuang 2010). As they rise, however, they become warmer than the environment. Therefore, clouds experience a smaller lapse rate than the environment, which means that $\partial q_v^*/\partial z$ is smaller in a cloud than in the environment. From Eq. (14), we see that a smaller $\partial q_v^*/\partial z$ will give a smaller γ. From Eq. (16), we see that a smaller $\partial q_v^*/\partial z$ will weight the integral in the denominator to smaller ρ and, therefore, will give a larger **w**. Since CAPE increases in these simulations as CO_2 is increased, we should expect these effects to be enhanced as the concentration of CO_2 goes up. This would tend to give the biases that we see.

To check this explanation for the bias in predicted γ and **w**, we recalculate the theoretical predictions using the profile of ρ and q_v^* for a saturated parcel lifted adiabatically from the cloud base. The resulting predictions are given by the red lines in Figs. 4 and 5. The effect is as expected: the predicted change in γ is smaller and the predicted change in **w** is larger. Although not perfect, the overall agreement between the theory (red lines) and the simulations (gray bars) is quite good, especially considering the simplifications in the theory. Since the properties of convection do not deviate significantly from the theory, the local precipitation fluxes roughly obey CC scaling. As discussed in section 1, this was not a foregone conclusion.

c. Dry spells

For fixed f, Eq. (8) tells us that na must scale like P_g/P_l. Since P_l grows faster with temperature than P_g, na must
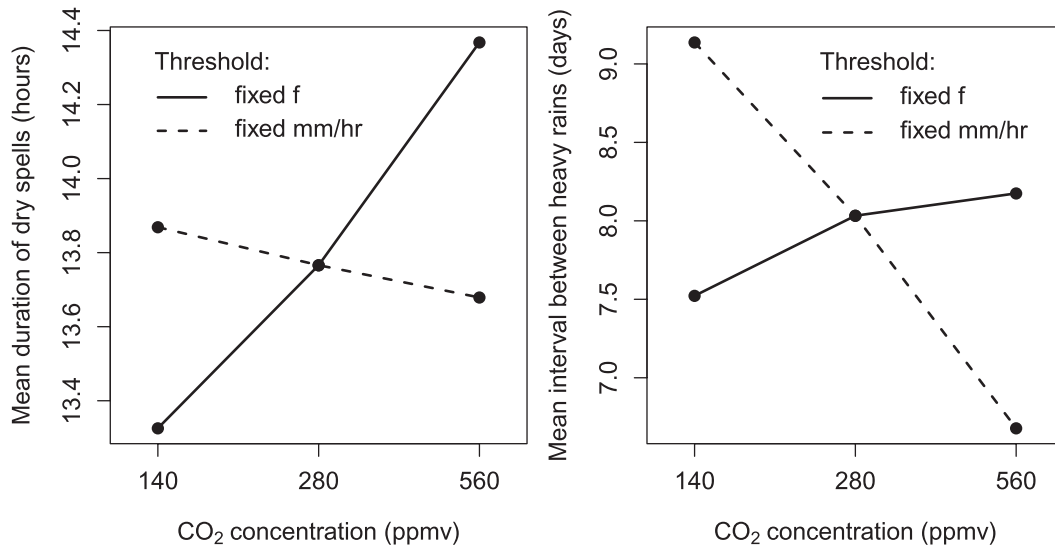
FIG. 6. (left) The mean duration of local dry spells, which are defined as the length of contiguous time during which the local precipitation flux is below the simulation's own $f = 90\%$ threshold $P_0(0.9)$ (fixed-f threshold, solid curve), or below the $P_0(0.9)$ threshold from the 280-ppmv simulation (fixed millimeter-per-hour threshold, dashed line). (right) As at (left), but for $f = 10\%$, which defines heavy rain events.

decrease with increasing CO_2. We might guess that the length of dry spells at a stationary point on the surface τ is proportional to one over this fractional area, that is, $\tau \propto 1/na$. This would imply longer dry spells with higher CO_2. The solid curves in Fig. 6 support this conclusion. In the left panel of Fig. 6, each point on the solid curve is the average length of time that $p < P_0(0.9)$ for a grid cell at the surface. We see that the duration of dry spells—as defined using this fixed-f threshold—increases with CO_2. The solid curve in the right panel is calculated using the fixed $f = 0.1$ threshold, which shows an increase in waiting time between the heaviest rain events. Quantitatively, however, $\tau \propto 1/na$ does not hold. For $f = 0.9$, $1/na$ increases by 5%–6% per doubling, but τ increases by only 3%–4%. Similarly, for $f = 0.1$, $1/na$ grows by 10%–12%, but τ grows by only 2%–7%. This deviation from proportionality can be caused by changes in cloud lifetimes or the speed with which clouds wander over the domain.

This issue of dry spells involves an important subtlety related to the choice of precipitation threshold. As temperature rises, so does $P_0(f)$ for fixed f. Therefore, a fixed-f threshold will become more restrictive as CO_2 increases, so it will produce larger increases in τ than would a fixed millimeter-per-hour threshold. To assess the importance of this effect, we can recalculate τ using a fixed millimeter-per-hour threshold set to $P_0(0.9)$ from the 280-ppmv simulation. Defined in this way, the duration of dry spells *decreases* with increasing CO_2 (dashed curve, left panel). Similarly, the waiting time between heavy precipitation events also decreases when using

a fixed millimeter-per-hour threshold (dashed curve, right panel).

d. Convective velocity

Let us take a closer look at the changes in cloud vertical velocity. The left panel of Fig. 7 plots $\log_{10}$ of the histogram of vertical velocity for the simulation with 280 ppmv of CO_2. At each height, the histogram is generated by taking each grid cell at every time step and binning it according to its vertical velocity. What we see in this figure are updrafts reaching speeds as high as about 35 m s^{-1} and downdrafts reaching speeds as high as about 13 m s^{-1}.

The right panel of Fig. 7 displays the ratio of the 560-ppmv histogram to the 280-ppmv histogram. The color scale ranges from deep blue corresponding to a ratio of 1 (i.e., no change) to deep red corresponding to an infinite ratio. White regions in the interior correspond to ratios less than 1. From the deep red colors at heights around 15 km, we see that convection has expanded to higher altitudes, which is expected since the radiative-cooling profile shifts upward with warming. What is more interesting is the fact that fast updrafts—i.e., those greater than 10 m s^{-1}—are more common at virtually all heights in the 560-ppmv simulation as compared to the 280-ppmv simulation. Throughout most of the troposphere, 15 m s^{-1} updrafts are about 50% more common and 20 m s^{-1} updrafts are about twice as common. This is a dramatic change in the behavior of convective updrafts. As a consequence of
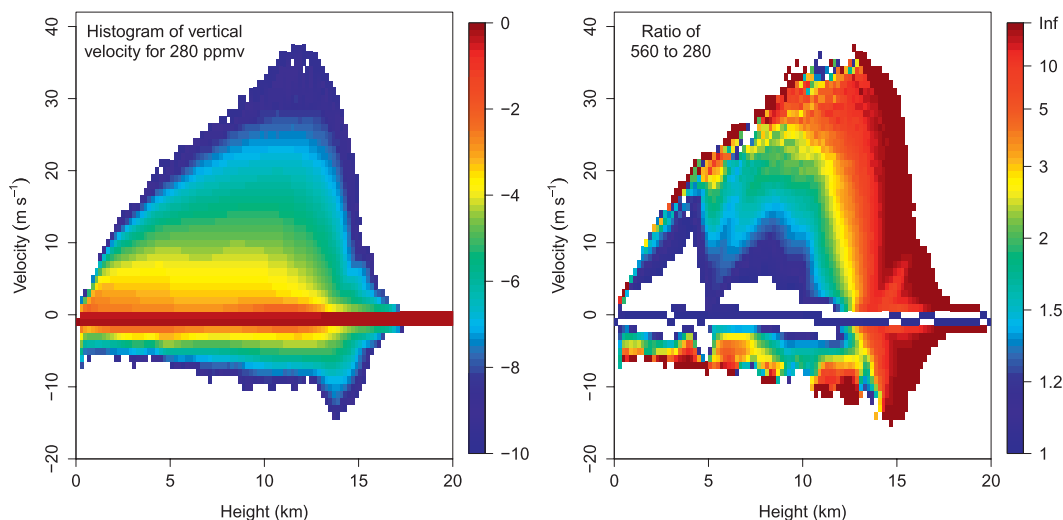
FIG. 7. (left) Log_{10} of the histogram of **w** for the simulation with 280 ppmv of CO_2. Each slice parallel to the ordinate is the frequency distribution of **w** at the corresponding height. (right) The ratio of the 560-ppmv histogram to the 280-ppmv histogram. The color bar ranges over the ratio r from 1 to ∞ with distance along the color bar proportional to $1 - 1/r$; ratios less than one show up as white.

this increased convective vigor, the anemonal[1] frictional dissipation, which takes a value of 1.7 W m^{-2} in the 280-ppmv simulation, increases by 9% for each of the two doublings. This agrees with the ~10% increase in dissipation found for a 3-K increase in SST in the RCE simulations of Romps (2008).

This increase in vertical velocity and dissipation coincides with an increase in CAPE. Calculating buoyancy for adiabatic ascent with the latent heat of fusion as shown in Fig. 1, CAPE increases by 6%–7% for each of the two doublings of CO_2. If the increase in CAPE is responsible for this overall increase in convective vigor, then the question shifts from ''Why do convective velocities increase?'' to ''Why does CAPE increase?'' Since we do not yet understand what sets CAPE in the current troposphere (i.e., why 1000 J kg^{-1} and not 100 or 10 000 J kg^{-1}?), the answer to this question may have to wait until a fundamental theory of moist convection is developed.

6. Summary and discussion

This paper presents the first results of a CO_2-doubling experiment in a high-resolution cloud-resolving model. When the preindustrial concentration of CO_2 is doubled, the sea surface temperature increases by 2.9 K, the global precipitation flux increases by 10% (3% K^{-1}),

and the local precipitation flux in the heaviest precipitation events increases by about 20% (7% K^{-1}), in rough agreement with Clausius–Clapeyron scaling. A set of IPAT-like identities [Eqs. (7) and (8)] are derived that relate the local and global precipitation fluxes to the properties of convection. A scaling theory is given for how these convective properties should change to be consistent with CC scaling of local precipitation fluxes [Eqs. (11)–(16)]. Although these convective properties (e.g., precipitation efficiency, cloud depth, cloud velocity) could have changed in ways to destroy CC scaling, they appear to behave in the simplest possible way—that is, in accordance with the scaling theory—and, therefore, preserve CC scaling (red lines and gray bars in Figs. 4 and 5). As predicted by the scaling theory, increases in CO_2 lead to more vigorous convection, composed of taller and faster plumes.

The finding that higher CO_2 leads to higher convective velocities contradicts the inferences from several GCM studies. In a simplified GCM, O'Gorman and Schneider (2009) found that increasing the longwave optical thickness of the atmosphere led to decreases in vertical-velocity variability in the tropics. This decrease in velocity variability was credited with decreasing the local precipitation fluxes. A similar conclusion was reached by Emori and Brown (2005), who found that, when CO_2 is increased in GCMs, the vertical-velocity variability decreases over most of the tropics, which tended to decrease precipitation fluxes. To understand the discrepancy between those two studies and the present one, it is important to note that the GCM studies were looking at the variability of vertical velocity at the GCM grid scale.

---

[1] Anemonal, meaning ''of or pertaining to the wind,'' refers here to the viscous dissipation of atmospheric motions, as opposed to the frictional heating by falling hydrometeors.

Tropical convective clouds, on the other hand, have much smaller scales, so we cannot assume that cloud vertical velocities are related in a simple way to the vertical velocity of the GCM grid scale.

Del Genio et al. (2007) approached this problem by calculating theoretical updraft speeds using a plume model and the atmospheric state provided by a GCM. With doubled CO_2, they found only small changes in the tropical updraft speeds. In particular, updrafts over the ocean with speeds greater than 7 m s^{-1} were found to occur only 0%–2% more often in a doubled-CO_2 climate. This is much less of an increase than is seen in the cloud-resolving simulations presented here. This discrepancy might be attributable to the simplifications in the plume model, or biases in the atmospheric state generated by the GCM's convective parameterization, or the lack of mesoscale and synoptic variability in the cloud-resolving simulations.

One of the downsides to the diagnostic approach used here is that the precipitation efficiency ϵ_p is defined to be independent of the threshold f. The assumption is that the fraction f of condensation that condenses at the highest rates produces the fraction f of precipitation that falls at the highest rates. In fact, there is good reason to suspect that this is not true. For example, shallow trade-wind cumuli are often nonprecipitating, which means that they have a precipitation efficiency close to zero. On the other hand, deep cumulonimbi generate higher concentrations of condensed water, which likely leads to more efficient rainout and, therefore, a precipitation efficiency that is likely larger than the global average of ~0.2.

Nevertheless, there are two reasons to believe that the assumption of an f-independent ϵ_p is satisfactory for our purposes. The first reason is that we are interested in the fractional changes of the terms in Eqs. (7) and (8), not their overall magnitudes. In other words, we may be using too large an A_c when studying $A_p(0.1)$ (i.e., too low a ϵ_p), but, if so, we are committing this same error in all three simulations. The second reason is that our choice of $\epsilon_p(0.9)$ cannot be wrong by more than about 10%: the worst-case scenario is that the 10% of condensation that was omitted was not associated with any precipitation. The fact that $f = 0.1$ gives results very similar to $f = 0.9$ lends the $f = 0.1$ results credibility and makes it unlikely that our choice of ϵ_p has introduced any significant error.

A contemporaneous study by Muller et al. (2011) has also investigated the behavior of local precipitation fluxes in a cloud-resolving simulation. They used a coarser grid spacing (4 km compared with 200 m) on a much larger domain (1024 km wide compared with 25.6 km wide) and they increased the fixed SST rather than increasing the concentration of CO_2 over a slab ocean. Nevertheless,

some of the conclusions are similar. For example, they find that the precipitation efficiency does not change with warming and that the local precipitation fluxes obey CC scaling. On the other hand, the convective velocities in their study decrease with warming in the lower half of the troposphere, leading to a reduction in condensation rates; the opposite conclusion is reached here.

APPENDIX A

Getting to Equilibrium

To achieve radiative–convective equilibrium in each simulation, a sequence of three different grids is used. The first grid uses a 2-km grid spacing in the horizontal and a stretched grid in the vertical; the domain is a cube with edge lengths of 32 km. This is followed by a grid with a 400-m grid spacing in the horizontal and a 200-m spacing in the vertical; the domain is a cube with edge lengths of 25.6 km. The third domain has the same cubic dimensions, but it uses a 200-m grid spacing in x, y, and z. These three domains will be referred to as the 2-km, 400-m, and 200-m grids.

The first simulation uses a CO_2 concentration of 280 ppmv to represent a preindustrial atmosphere. This simulation begins on a 2-km grid with a fixed SST of 300 K. This simulation is run for several years to ensure that a steady state has been reached. Since this run uses a fixed SST, the energy budget of the ocean is not closed. In fact, the ocean is a significant sink of energy by virtue of the fact that the net downwelling radiation at the surface exceeds the latent and sensible heat fluxes. In this first simulation, the ocean serves as a sink for 105.5 W m^{-2}.

Since the energy budget of the atmosphere is closed in a steady state, 105.5 W m^{-2} is the net radiative imbalance of the ocean and atmosphere system. This radiative imbalance is similar to the rate diagnosed by Tian et al. (2001) for the Tropical Ocean and Global Atmosphere Coupled Ocean–Atmosphere Response Experiment (TOGA COARE) campaign over the western Pacific warm pool. They found that the net downward radiative flux at the top of the atmosphere was about 110 W m^{-2} with uncertainties of about 10 W m^{-2}. That was apportioned into 80 W m^{-2} of atmospheric export and 30 W m^{-2} of oceanic transport. In the cloud-resolving model, there is no opportunity for atmospheric export of energy, so the entire radiative imbalance must go into the ocean.

The simulation is then restarted on the 400-m grid by interpolating the atmospheric state to this higher resolution. After 50 days, the net enthalpy flux into the ocean is diagnosed as 120 W m^{-2}. Note that this is substantially higher than the 105.5 W m^{-2} diagnosed in the 2-km run. The simulation is then run on the 200-m grid for 44 days and a flux of 120 W m^{-2} is diagnosed once again, suggesting that this ocean flux has converged as a function of grid spacing. Next, the simulation is restarted on the same 200-m grid, but the fixed-SST ocean is replaced by a slab ocean with an applied heat sink of 120 W m^{-1}. This slab-ocean part of the simulation is run to equilibrium for 146 days.

The slab ocean is assumed to have a constant depth of 10 m regardless of the exchange of water vapor or liquid water with the atmosphere; in this sense, the slab ocean does not conserve mass. Energy, on the other hand, is conserved by equating the change in the slab's internal energy with the net enthalpy fluxes into the ocean (including those from radiation, evaporation, conduction, precipitation, and the applied heat sink). The entire slab is also treated as having a single temperature, so that changes in its temperature are attributable to the sum of enthalpy fluxes over its entire surface. Physically, this slab ocean may be thought of as being well mixed. By reducing the effect of local cloud shading in this way, we get an ocean that behaves like a much deeper ocean, but with the benefit of a faster equilibration time.

The other two simulations—one with 140-ppmv CO$_2$ and the other with 560-ppmv CO$_2$—are run exclusively over the slab ocean. First, both of these simulations are run on a 2-km grid for years in order to reach a steady state. The heat sink applied to the ocean in these simulations is the 105.5 W m^{-2} diagnosed from the fixed 300-K-SST simulation performed on the same 2-km grid. Next, the simulations are restarted on a 400-m grid and run for about 50 days using the 120 W m^{-2} diagnosed from the fixed 300-K SST simulation performed on the 400-m grid. Finally, the simulations are restarted on the 200-m grid using, once again, the 120 W m^{-2} heat sink. These high-resolution simulations are run for well over 100 days. On occasion, the temperature of the slab ocean is adjusted by hand to expedite the approach to equilibrium.

The last year of the SST time series is shown in Fig. A1 for each of the three simulations. The black, green, and blue lines correspond to the 2-km, 400-m, and 200-m grids, respectively. The dashed lines are those parts of the 280-ppmv simulation run over a fixed SST of 300 K, and the solid lines are those parts of the simulations run over a slab ocean. The vertical red lines denote the times when the temperature of the slab ocean was changed by hand to speed the approach to a steady state.
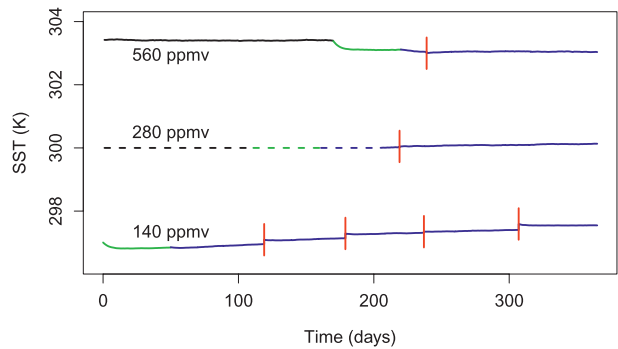
FIG. A1. The SST time series for the last year of each of the three simulations. The three colors of the curves correspond to a horizontal grid spacing of 2 km (black), 400 m (green), and 200 m (blue). Dashed lines correspond to a fixed SST of 300 K and solid lines correspond to a slab ocean. Red lines denote times when the SST was shifted by hand to speed convergence.

APPENDIX B

The IPAT Equation

To measure the properties of convecting clouds, we must decide how to take averages in the volume above $A_c(f)$. One approach would be to take volume-weighted averages where the condensate mixing ratio q_c is positive. For example, we might try to define the mean density of convecting clouds as

$$\frac{\int_{A_c} dt\, dx\, dy \int_{q_c>0} dz \rho}{\int_{A_c} dt\, dx\, dy \int_{q_c>0} dz}.$$

This has the obvious deficiency of including nonconvecting cloud in the integral. One way around this problem would be to calculate a volume-weighted mean over only air that is condensing, such as

$$\frac{\int_{A_c} dt\, dx\, dy \int_{c>0} dz \rho}{\int_{A_c} dt\, dx\, dy \int_{c>0} dz},$$

where the condensation rate c is the microphysical sink of water vapor attributable to condensation and deposition in dimensions of mass per volume per time. The problem with this averaging approach is that lightly condensing air parcels are given the same weight as heavily condensing parcels. For example, this quantity could be changed significantly by an increase in the volume of lightly condensing, transient, in situ clouds, which do not contribute any precipitation. The solution

is to weight clouds not by their volume, but by their contribution to the hydrologic cycle; that is, their condensation rate c. In particular, we define $\langle F \rangle$ as the condensation-weighted average of $F = F(x, y, z, t)$ in the volume of atmosphere above A_c,

$$\langle F \rangle = \frac{\int_{A_c} dt \, dx \, dy \int dz c F}{\int_{A_c} dt \, dx \, dy \int dz c}. \tag{B1}$$

For a particular RCE, $\langle F \rangle$ is a function only of the precipitation fraction f.

With this condensation-weighted average, we start with the mean advection term $\langle -\rho w \partial q_v / \partial z \rangle$ and follow the same set of steps outlined for a single column in section 3. Since we are now averaging over 4D space–time instead of a 1D column, we naturally obtain a definition for the hypervolume of convecting cloud V rather than the depth H. The set of definitions that we obtain are as follows:

$$\text{Total convecting cloud hypervolume} = V \equiv \frac{\int_{A_c} dt \, dx \, dy \int dz c}{\langle c \rangle},$$

$$\text{Number density of precipitation events} = n \equiv \frac{\int dt (\text{Number of connected spaces in } A_p \text{ at } t)}{\int dt \, dx \, dy},$$

$$\text{Area of a precipitation event} = a \equiv \frac{\int_{A_p} dt \, dx \, dy}{n \int dt \, dx \, dy},$$

$$\text{Precipitation efficiency} = \epsilon_p \equiv \frac{f P_g \int dt \, dx \, dy}{V \langle c \rangle},$$

$$\text{Condensation efficiency} = \epsilon_c \equiv \frac{\langle c \rangle}{\left\langle -\rho w \dfrac{\partial q_v}{\partial z} \right\rangle},$$

$$\text{Water-vapor gradient} = \gamma \equiv \frac{\left\langle -\rho w \dfrac{\partial q_v}{\partial z} \right\rangle}{\langle \rho w \rangle},$$

$$\text{Convecting cloud mass} = m \equiv \frac{\langle \rho \rangle V}{\int_{A_p} dt \, dx \, dy}, \quad \text{and}$$

$$\text{Convecting cloud velocity} = \mathbf{w} \equiv \frac{\langle \rho w \rangle}{\langle \rho \rangle}. \tag{B2}$$

With these definitions, Eqs. (7) and (8) are identities.

An alternative definition for n can be obtained by calculating the equivalent number of equal-radius circles in A_p. A number density n of circles with radius r will have an area density of $n\pi r^2$ and a perimeter density of $n2\pi r$. Equating these to the area density and perimeter density of A_p, we obtain an equivalent-circle definition,

$$n \equiv \frac{\left[\int dt (\text{Perimeter length of } A_p \text{ at } t) \right]^2}{4\pi \left(\int dt \, dx \, dy \right) \left(\int_{A_p} dt \, dx \, dy \right)}.$$

As it turns out, the connected-space definition of n is equal to about two-thirds that of the equivalent-circle

definition for both $f = 0.9$ and $f = 0.1$. More importantly, these two definitions agree to within a few percent on the fractional changes in n from one simulation to the next. Since the connected-space definition is more intuitive, it is the one used in this paper.

In practice, the quantities in Eq. (B2) are calculated by saving two-dimensional arrays of the following quantities averaged over 5-min intervals:

$$p, \int dz c, \int dz c^2, \int dz c \rho w \frac{\partial q_v}{\partial z}, \int dz c \rho, \quad \text{and} \quad \int dz c \rho w.$$

Here, p is the precipitation flux at the surface with dimensions of mass per area per time. During the last 40 days of each simulation, these arrays are saved every

5 min, producing a total of 11 520 arrays for each of these six quantities. Using either $f = 0.9$ or $f = 0.1$, a single threshold P_0 is calculated from all 11 520 arrays of the p data, and likewise for C_0 from the $\int dzc$ data. Given these two thresholds, the subsets A_c and A_p are then defined for each 5-min interval and the quantities in Eq. (B2) are calculated.

REFERENCES

Allen, M. R., and W. J. Ingram, 2002: Constraints on future changes in climate and the hydrologic cycle. *Nature,* **419,** 224–232.

Boer, G., 1993: Climate change and the regulation of the surface moisture and energy budgets. *Climate Dyn.,* **8,** 225–239.

Bretherton, C., 2007: Challenges in numerical modeling of tropical circulations. *The Global Circulation of the Atmosphere,* T. Schneider and A. H. Sobel, Eds., Princeton University Press, 302–330.

Ciesielski, P. E., R. H. Johnson, P. T. Haertel, and J. Wang, 2003: Corrected TOGA COARE sounding humidity data: Impact on diagnosed properties of convection and climate over the warm pool. *J. Climate,* **16,** 2370–2384.

Clough, S., M. Shephard, E. Mlawer, J. Delamere, M. Iacono, K. Cady-Pereira, S. Boukabara, and P. Brown, 2005: Atmospheric radiative transfer modeling: A summary of the AER codes. *J. Quant. Spectrosc. Radiat. Transfer,* **91,** 233–244.

Commoner, B., 1971: *The Closing Circle: Nature, Man, and Technology.* Knopf, 326 pp.

Del Genio, A. D., M.-S. Yao, and J. Jonas, 2007: Will moist convection be stronger in a warmer climate? *Geophys. Res. Lett.,* **34,** L16703, doi:10.1029/2007GL030525.

Ehrlich, P. R., and J. P. Holdren, 1972: A bulletin dialogue on "The Closing Circle": Critique. *Bull. At. Sci.,* **28,** 16–27.

Emori, S., and S. J. Brown, 2005: Dynamic and thermodynamic changes in mean and extreme precipitation under changed climate. *Geophys. Res. Lett.,* **32,** L17706, doi:10.1029/2005GL023272.

Gordon, H., P. Whetton, A. Pittock, A. Fowler, and M. Haylock, 1992: Simulated changes in daily rainfall intensity due to the enhanced greenhouse effect: Implications for extreme rainfall events. *Climate Dyn.,* **8,** 83–102.

Hartmann, D. L., and K. Larson, 2002: An important constraint on tropical cloud–climate feedback. *Geophys. Res. Lett.,* **29,** 1951, doi:10.1029/2002GL015835.

Held, I., and B. Soden, 2006: Robust responses of the hydrological cycle to global warming. *J. Climate,* **19,** 5686–5699.

Hennessy, K., J. Gregory, and J. Mitchell, 1997: Changes in daily precipitation under enhanced greenhouse conditions. *Climate Dyn.,* **13,** 667–680.

Iacono, M. J., J. S. Delamere, E. J. Mlawer, M. W. Shephard, S. A. Clough, and W. D. Collins, 2008: Radiative forcing by long-lived greenhouse gases: Calculations with the AER radiative transfer models. *J. Geophys. Res.,* **113,** D13103, doi:10.1029/2008JD009944.

Iwashima, T., and R. Yamamoto, 1993: A statistical analysis of the extreme events: Long-term trend of heavy daily precipitation. *J. Meteor. Soc. Japan,* **71,** 637–640.

Karl, T., R. Knight, and N. Plummer, 1995: Trends in high-frequency climate variability in the twentieth century. *Nature,* **377,** 217–220.

Kharin, V., F. Zwiers, X. Zhang, and G. Hegerl, 2007: Changes in temperature and precipitation extremes in the IPCC ensemble of global coupled model simulations. *J. Climate,* **20,** 1419–1444.

Krueger, S., Q. Fu, K. Liou, and H. Chin, 1995: Improvements of an ice-phase microphysics parameterization for use in numerical simulations of tropical convection. *J. Appl. Meteor.,* **34,** 281–287.

Leonard, B. P., M. K. MacVean, and A. P. Lock, 1993: Positivity-preserving numerical schemes for multidimensional advection. NASA Tech. Rep. 106055, 62 pp.

Lin, Y., R. Farley, and H. Orville, 1983: Bulk parameterization of the snow field in a cloud model. *J. Climate Appl. Meteor.,* **22,** 1065–1092.

Lindzen, R., M. Chou, and A. Hou, 2001: Does the Earth have an adaptive infrared iris? *Bull. Amer. Meteor. Soc.,* **82,** 417–432.

Lord, S., H. Willoughby, and J. Piotrowicz, 1984: Role of a parameterized ice-phase microphysics in an axisymmetric, nonhydrostatic tropical cyclone model. *J. Atmos. Sci.,* **41,** 2836–2848.

Meehl, G. A., C. Covey, T. Delworth, M. Latif, B. McAvaney, J. F. B. Mitchell, R. J. Stouffer, and K. E. Taylor, 2007: The WCRP CMIP3 multimodel dataset: A new era in climate change research. *Bull. Amer. Meteor. Soc.,* **88,** 1383–1394.

Muller, C. J., P. A. O'Gorman, and L. E. Back, 2011: Intensification of precipitation extremes with warming in a cloud-resolving model. *J. Climate,* in press.

O'Gorman, P. A., and T. Schneider, 2009: Scaling of precipitation extremes over a wide range of climates simulated with an idealized GCM. *J. Climate,* **22,** 5676–5685.

Pall, P., M. Allen, and D. Stone, 2007: Testing the Clausius–Clapeyron constraint on changes in extreme precipitation under CO_2 warming. *Climate Dyn.,* **28,** 351–363.

Ramanathan, V., 1981: The role of ocean–atmosphere interactions in the CO_2 climate problem. *J. Atmos. Sci.,* **38,** 918–930.

Romps, D. M., 2008: The dry-entropy budget of a moist atmosphere. *J. Atmos. Sci.,* **65,** 3779–3799.

——, and Z. Kuang, 2010: Do undiluted convective plumes exist in the upper tropical troposphere? *J. Atmos. Sci.,* **67,** 468–484.

Sun, Y., S. Solomon, A. Dai, and R. Portmann, 2007: How often will it rain? *J. Climate,* **20,** 4801–4818.

Suppiah, R., 1994: Synoptic aspects of wet and dry conditions in central Australia: Observations and GCM simulations for 1 × CO_2 and 2 × CO_2 conditions. *Climate Dyn.,* **10,** 395–405.

Thuburn, J., 1996: Multidimensional flux-limited advection schemes. *J. Comput. Phys.,* **123,** 74–83.

Tian, B., G. Zhang, and V. Ramanathan, 2001: Heat balance in the Pacific warm pool atmosphere during TOGA COARE and CEPEX. *J. Climate,* **14,** 1881–1893.

Tompkins, A., and G. Craig, 1999: Sensitivity of tropical convection to sea surface temperature in the absence of large-scale flow. *J. Climate,* **12,** 462–476.

Trenberth, K., A. Dai, R. Rasmussen, and D. Parsons, 2003: The changing character of precipitation. *Bull. Amer. Meteor. Soc.,* **84,** 1205–1217.

Yanai, M., S. Esbensen, and J.-H. Chu, 1973: Determination of bulk properties of tropical cloud clusters from large-scale heat and moisture budgets. *J. Atmos. Sci.,* **30,** 611–627.